Temperature Dependence of Transport Properties of Spiro-MeOTAD as a Hole Transport Material in Solid-State Dye-Sensitized Solar Cells

Amalie Dualeh, Thomas Moehl,* Mohammad Khaja Nazeeruddin, and Michael Grätzel*

Laboratory of Photonics and Interfaces, Institute of Chemical Sciences and Engineering, École Polytechnique Fédérale de Lausanne, Lausanne, Switzerland

ABSTRACT The internal transport and recombination parameters of solid-state dye-sensitized solar cells (ssDSCs) using the amorphous organic semiconductor 2,2′,7,7′-tetrakis(*N*,*N*-di-*p*-methoxyphenylamine)-9,9′-spirobifluorene (spiro-MeOTAD) as a hole transport material (HTM) are investigated using electrical impedance spectroscopy. Devices were fabricated using flat and nanostructured TiO_2 and compared to systems using nanostructured ZrO_2 to differentiate between the transport processes within the different components of the ssDSC. The effect of chemically p-doping the HTM on its transport was investigated, and its temperature dependence was examined and analyzed using the Arrhenius equation. Using this approach the activation energy of the hole hopping transport within the undoped spiro-MeOTAD film was determined to be 0.34 ± 0.02 and 0.40 ± 0.02 eV for the mesoporous TiO_2 and ZrO_2 systems, respectively.

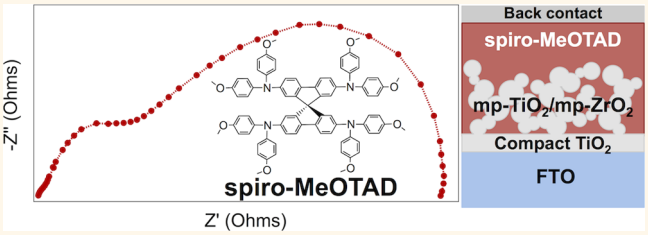

KEYWORDS: photovoltaic devices · dye-sensitized solar cells · hole transport material · electrical impedance spectroscopy · charge transport

The dye-sensitized solar cell (DSC)[1] is a promising alternative to conventional silicon-based photovoltaic devices. In this system a mesoporous semiconductor (commonly titanium dioxide, TiO_2) is sensitized by a light-absorbing dye that when exposed to sunlight is photoexcited. After light absorption the excited dye molecules inject the electron into the semiconductor and are regenerated by a redox electrolyte. The highest power conversion efficiency (PCE) of 12.3% has been achieved using a porphyrin sensitizer in combination with a cobalt(II)/(III) redox electrolyte.[2]

In an effort to improve the stability and processability of DSCs with the aim to allow efficient roll-to-roll manufacturing, extensive research is being invested in the study of solid and quasi-solid alternatives for the liquid electrolyte. Efforts have focused on organic[3−7] and inorganic[8−10] semiconductors and conducting polymers[11,12] in order to meet all the requirements for a good hole transport material (HTM). In the field of organic semiconductors, the p-type semiconductor 2,2′,7,7′-tetrakis(*N*,*N*-di-*p*-methoxyphenylamine)-9,9′-spirobifluorene (spiro-MeOTAD)[13] (Figure 1) remains the material of choice for high PCEs. Electrochemical impedance spectroscopy (EIS) has become a powerful tool used to characterize the internal electrical processes occurring within devices such as dye-sensitized solar cells. The attraction of this technique is the possibility to probe the individual interfaces within the devices and the corresponding charge transfer phenomena and thus gain an insight into the dynamics within the working device.

In this work EIS was used to study the transport properties of the organic p-type semiconductor spiro-MeOTAD and its dependence on temperature. The effect of temperature on the transport of spiro-MeOTAD and thus the overall device performance has significant importance, due to the large range of temperatures devices are subjected to in real-life application. Previous studies[14,15] examined the effect of varying the temperature on the electrical parameters of liquid DSCs and observed decreases in the

* Address correspondence to thomas.moehl@epfl.ch; michael.graetzel@epfl.ch.

Received for review November 23, 2012 and accepted February 27, 2013.

Published online February 27, 2013
10.1021/nn4005473

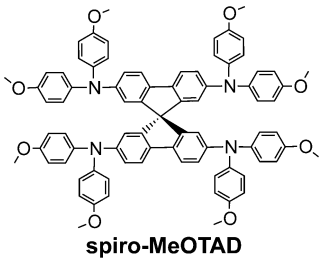

Figure 1. Molecular structure of the HTM, spiro-MeOTAD.

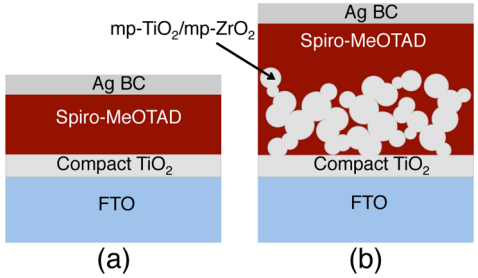

Figure 2. Schematic illustration of the device structures for compact TiO_2 with (a) spiro-MeOTAD deposited directly and (b) mesoporous (mp) ZrO_2 or TiO_2 infiltrated with spiro-MeOTAD. Fluorine-doped tin oxide (FTO) glass substrates and silver back contacts (Ag BC) were used to complete the devices.

electron lifetimes as a function of temperature in liquid DSCs. Furthermore temperature variations were found to have restoring effects[16] on the device performance of DSCs with liquid and semisolid electrolytes. In the case of DSCs using solid-state electrolytes, the influence of environmental factors such as temperature on the electrical parameters of the device performance has been studied relatively little so far and is not fully understood.

EIS has been used extensively to study liquid DSCs,[17−20] and the physical mechanisms of charge transfer in this system are well understood. In the case where the liquid electrolyte is replaced by a solid-state hole transport material, the model used to fit liquid DSCs is no longer completely sufficient and requires adjustment. Previous work[21−23] considered the electron and the hole transport through the use of a two-channel transmission line model in order to fit the transport characteristics that appear when a more resistive electrolyte (such as a solid HTM) is employed. In order to better understand the processes occurring within ssDSCs, three different systems were investigated: compact TiO_2 with (1) spiro-MeOTAD deposited directly on top and (2) mesoporous ZrO_2 or (3) mesoporous TiO_2 infiltrated with the HTM, as depicted in Figure 2. The first-case scenario models the direct interface between the HTM and the semiconductor material (here TiO_2). However in the case of real devices this simplistic model is further complicated due to the convoluted mesoporous structure of the nanocrystalline semiconductor. To simulate a three-dimensional HTM matrix, mesoporous ZrO_2 was chosen because of its insulating character, which prevents current flowing over the mesoporous matrix and thus simply acting as a scaffold for the HTM. Finally case 3 represents the real case scenario within working ssDSCs where the HTM infiltrates a mesoporous TiO_2 film. No sensitizer was used in these devices to simplify the interfaces being considered.

In its pristine state, spiro-MeOTAD has low conductivity, and thus in order to achieve high efficiencies in ssDSCs, the material needs to be p-doped to increase the charge carrier density. While this occurs naturally during exposure to oxygen and light (so-called photodoping), a range of chemical dopants have been investigated to controllably oxidize the spiro-MeOTAD, making it sufficiently conductive to achieve PCEs. Li-$(CF_3SO_2)_2N$ (LiTFSI) is conventionally used as an additive to the HTM to increase its conductivity.[24] Recent studies have found that it further plays a significant role in the doping process of the spiro-MeOTAD,[25,26] where the Li^+ is believed to be consumed during the oxidation process, which may compromise the device's long-term stability. To achieve high PCEs under controlled conditions, in addition to LiTFSI a cobalt(III) complex, coded FK-102,[27] was used to chemically p-dope the HTM during the manufacture of the devices. In this work the effect of chemically doping spiro-MeOTAD on its transport properties was investigated.

RESULTS AND DISCUSSION

Normally the general equivalent circuit used to model ssDSCs uses an adapted transmission line to describe the diffusion−recombination limited transport within the mesoporous semiconductor and the transport within the HTM.[22] The samples from Fabregat *et al.*[22] were not sealed, and therefore the properties of the device components, especially the HTM, can change rapidly during the EIS measurement. The model used in the work of Fabregat *et al.*[22] is the two-channel transmission line with both channels open, corresponding to the transport in the wide band gap semiconductor and in the HTM, respectively. In the case examined in this study the channel for the HTM was not used. The transport of the HTM is simply modeled by a resistor. This is a very similar model to that used by Boix *et al.*[28] for organic/inorganic hybrid solar cells using TiO_2/Sb_2S_3/P3HT. An example of the Nyquist plots is presented in Figure 3. The spectral features could be categorized into different frequency ranges. The resistance of the conducting glass, contacts, and wires, R_S, can be determined from the intersection of the first arc at high frequency, labeled region I. The arc at high frequency was independent of applied bias regardless of the system under consideration and was attributed to the charge transfer resistance (R_C) and the interfacial capacitance at the back

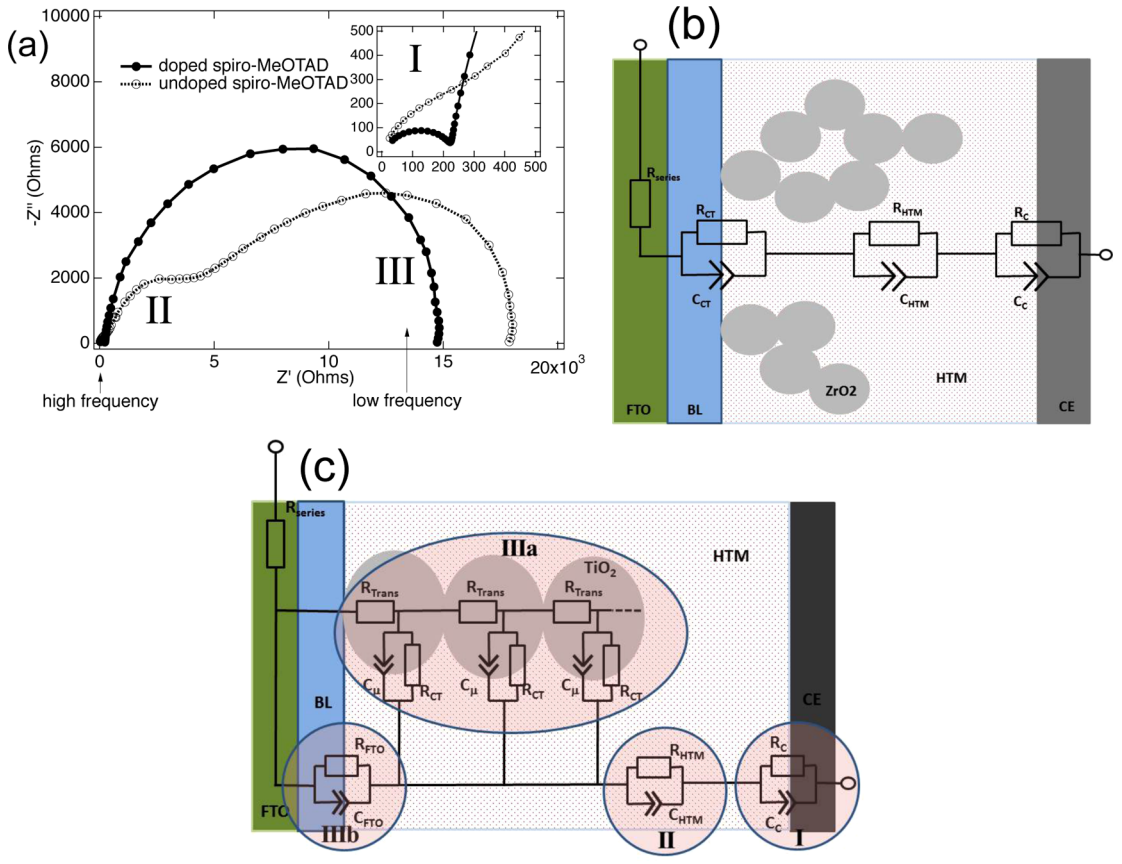

Figure 3. (a) Nyquist plots measured under dark at 0.65 V for devices using mesoporous TiO_2 infiltrated with doped (solid line) and undoped (dashed line) spiro-MeOTAD. This measurement was conducted at 0 °C. The inset shows detail of the high-frequency region. Corresponding equivalent circuit models used to fit the EIS data for systems using the (b) mesoporous ZrO_2 and (c) mesoporous TiO_2. BL = compact TiO_2 blocking layer; CE = Ag back contact used as counter electrode.

contact (BC)/HTM interface. The RC arc at low frequency, region III, was identified as the recombination resistance, R_{ct}, of electrons in the TiO_2 and holes in the HTM and the corresponding chemical capacitance, C_μ. The arc at intermediate frequency, region II, was observed to merge with the low-frequency arc as well as overlapping slightly with the high-frequency arc. This feature has been ascribed to the charge transport resistance, R_{HTM}, and capacitance of the HTM. This phenomena is clearly visible down to low forward potentials, and as such it is not an artifact resulting from the fitting procedure; see Figure 4. In the case of the mesoporous TiO_2 samples, there is a straight line feature, at the intersection between regions II and III, which is attributed to the transmission line (see section IIIa in Figure 3c), from which the transport resistance of electrons in the TiO_2 can be determined at high forward bias. This feature was often observed to be partially hidden beneath the high degree of overlap between the arc corresponding to R_{HTM} (see Figure 3), making it difficult to fit the transport resistance of the TiO_2 reliably. Section IIIb of the equivalent circuit model in Figure 3c was used to fit the low forward bias region when the TiO_2 is not conductive and the current flows over the compact TiO_2 layer/HTM interface. At high forward bias only the capacitive element of feature IIIb is still active.

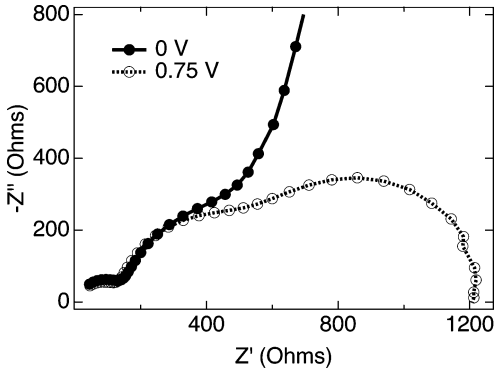

Figure 4. Nyquist plots measured under dark at 0 V (dashed line) and 0.75 V (solid line) for devices using mesoporous ZrO_2 infiltrated with undoped spiro-MeOTAD. This measurement was conducted at 20 °C.

In the case where devices were fabricated using mesoporous ZrO_2 this straight line feature is not present due to the insulating character of the ZrO_2; see Figure 4. However the continued presence of an intermediate frequency arc indicates that the charge transport resistance of the HTM can be modeled as a characteristic feature separate from the transmission

line, validating the use of an additional RC element in series to the transmission line for this parameter similar to the EIS analysis of Boix *et al.*,[28,29] see Figure 3b. The equivalent circuit presented in Figure 3b also applies to the model used to fit the low forward bias region of devices with mesoporous TiO_2. This is based on the fact that under these conditions the TiO_2 is insulating.

The transport resistance of the electrons in the TiO_2, as a property that is associated with the material of the metal oxide semiconductor and not the HTM, is, in this work, not of primary interest. Due to the deviation from ideality of these devices, constant phase elements were used instead of ideal capacitors to fit the data with the proposed models.

It was observed that upon p-doping the spiro-MeOTAD, the intermediate arc, region II, decreased significantly in magnitude and even vanished, indicating that the corresponding resistance decreased. This confirms again the association of this feature with the transport within the HTM, as the process of chemical p-doping leads to the creation of additional holes, increasing the doping inside the HTM and hence its conductivity explaining the decrease in R_{HTM}.

Using this model to analyze the EIS spectra, the effect of temperature on the individual processes was examined in order to gain a better understanding of the mechanisms within the working devices.

Interpretation of EIS Spectra. The trend observed for the charge transfer resistance at the BC/HTM interface, R_C, and the corresponding capacitance was found to be similar for the different systems, regardless if the film consisted of solely flat TiO_2 or had an additional layer of mesoporous TiO_2 or ZrO_2; see Figure 5. As previously stated, R_C was found to be mainly independent of the applied bias, indicating that it does not depend directly on the Fermi level position. As such, taking into account the potential drop due to the series resistance does not change the observed trends (see Supporting Information Figure 3). Furthermore the magnitude of the resistance decreased with increasing temperature, while the magnitude of the corresponding capacitance was found to increase as expected, Figure 5. At high temperature the resistance no longer remained independent of the applied potential, and showed after a slight decrease (increase) at high forward potentials an increase (decrease) in the capacitance.

The second arc, found at intermediate frequency (region II in Figure 3a), representing the charge transport resistance, R_{HTM}, and capacitance of the HTM, was found to substantially decrease and even disappear upon chemically p-doping the HTM; see Figure 3. The resistance corresponding to the hole transport in spiro-MeOTAD contributes to the total series resistance of the devices and hence greatly influences the fill factor (FF) of ssDSCs. The decrease in R_{HTM} upon doping spiro-MeOTAD is a major factor in the observed increase in the FF upon doping the HTM.[27] Consequently it was not possible to determine the R_{HTM} for samples prepared with doped spiro-MeOTAD. In the cases of undoped samples, the magnitude of the resistance was found to remain relatively constant with applied potential and decrease with increasing temperature, Figure 6. Hence similarly to the case of the charge transfer resistance at the BC/HTM interface, the observed trends do not change when the ohmic drop is taken into account and the corrected potential is used (see Supporting Information Figure 4) in place of the applied potential.

The associated capacitance was found to decrease slightly at high potentials (Figure 6), this effect being more pronounced in the case of the mesoporous ZrO_2 samples compared to the mesoporous TiO_2. Previous studies[30,31] measuring the transport time of ssDSCs by transient photovoltage and photocurrent decay showed this parameter to increase at high forward bias when conducted under high light intensities. A similar observation is made here, where R_{HTM} is seen to increase at high forward bias for measurements at higher temperatures. While not fully understood, this effect appears only when the HTM is already very conductive, either due to increased temperatures or at higher light intensities or forward potentials.

The transport electrons within the nanostructured metal oxide semiconductor in DSCs have been expressed in terms of the diffusion−recombination transmission line model.[21,20,32] The transport resistance, R_t, can be determined from the turnover between the diffusion feature, observed as a 45° line at high frequency, and the curvature of the low-frequency recombination arc.[20] It has been observed that the intermediate arc, corresponding to the hole transport in spiro-MeOTAD, merges with the recombination resistance feature at low frequency (region III in Figure 3a) for the samples considered here. This suggests that the time scales for these processes are relatively close, consequently partially hiding the straight line feature corresponding to the electron transport. An example of the electron transport resistance determined using the transmission line model is presented in the Supporting Information Figure 1. The transmission line is often clearly visible only at one or two potentials, and therefore the error associated with R_t is large. As previously described, section IIIb of the equivalent circuit model in Figure 3c was used to fit the low forward bias region when the TiO_2 is not conductive and recombination occurs *via* the compact TiO_2 blocking layer/HTM interface. At high forward bias recombination occurs across the transmission line as shown in section IIIa.

In the case of ZrO_2, the conduction band position is assumed to be sufficiently high that there is no injection of charge carriers to or from spiro-MeOTAD.

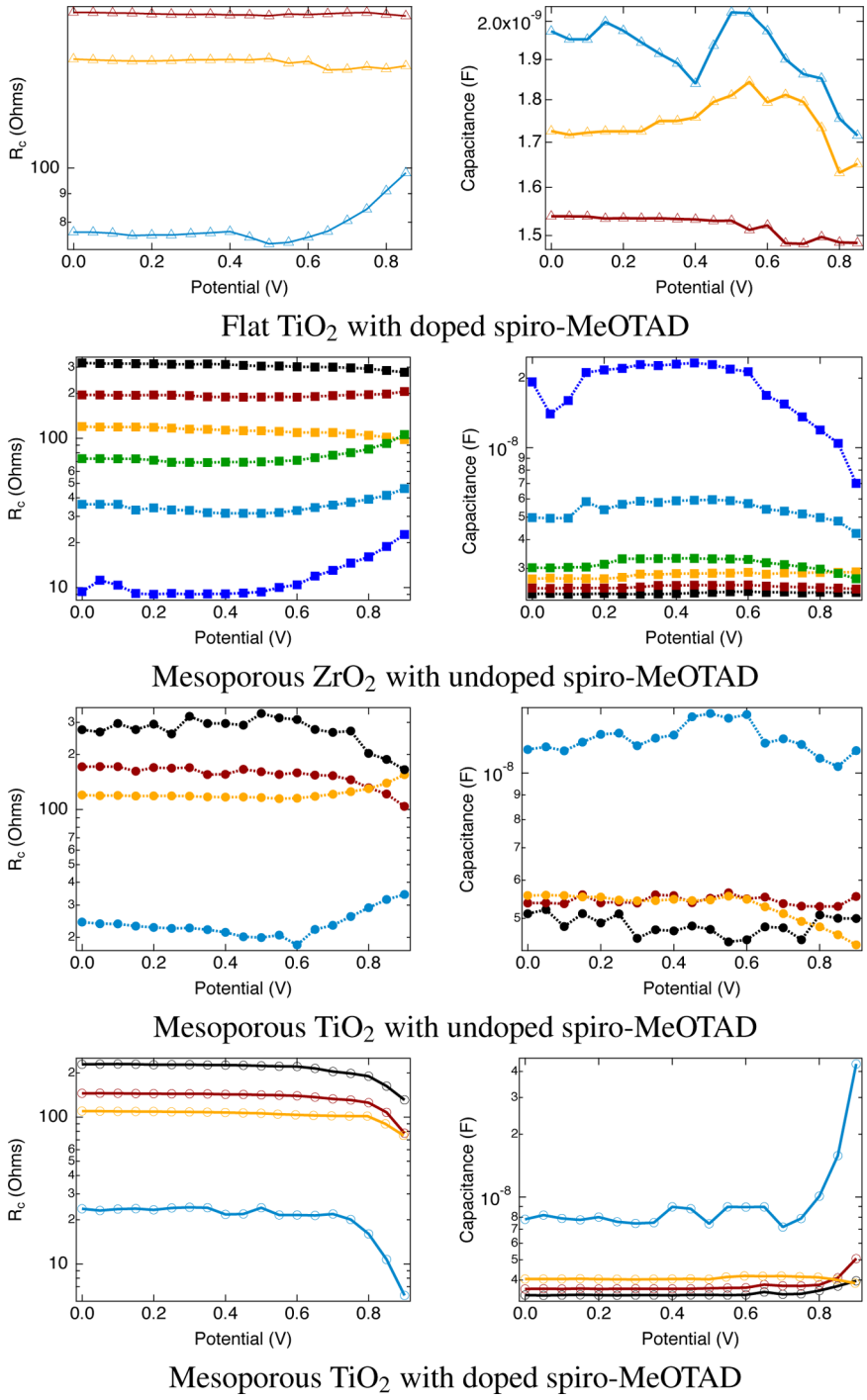

Figure 5. Charge transfer resistance and the corresponding capacitance at the BC/HTM interface for the different systems as a function of potential. Measurement temperatures: black (0 °C), red (10 °C), orange (20 °C), green (30 °C), light blue (40 °C), dark blue (50 °C).

The charge transport within organic semiconductors such as spiro-MeOTAD has been found to be in agreement with the Bässler formalism, which describes the transport to occur *via* hole hopping through localized states.[33] Here we assume the frequency of hole hopping transport in the HTM to be proportional to its conductivity. Assuming that the concentration of the charge carriers is constant, this frequency of hole hopping (k) is inversely proportional to the charge transport resistance of the HTM, which was determined by EIS above. Hence the activation energy (E_A) for the hole hopping transport in spiro-MeOTAD can be determined using the Arrhenius equation:

$$k = A \exp\left[\frac{E_A}{k_B T}\right] \propto \frac{1}{R_{HTM}} \qquad (1)$$

where A is the pre-exponential factor, k_B is the Boltzmann factor, and T is the temperature.

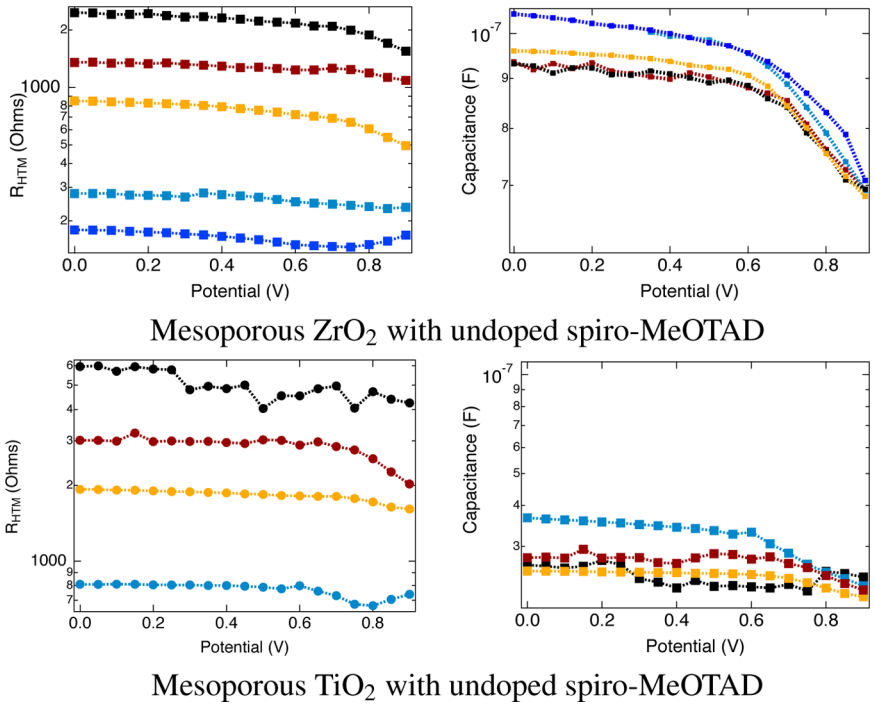

Figure 6. Charge transport resistance, R_{HTM}, and capacitance of the HTM for mesoporous ZrO_2 and TiO_2 as a function of potential. Measurement temperatures: black (0 °C), red (10 °C), orange (20 °C), light blue (40 °C), dark blue (50 °C).

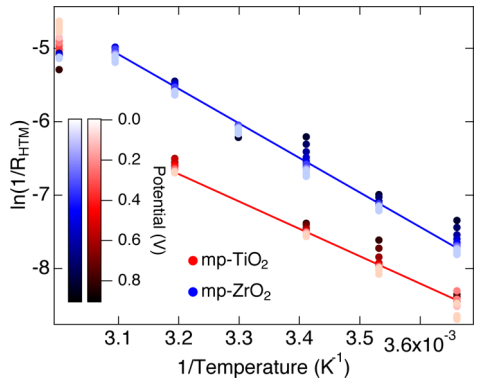

Figure 7. Arrhenius plot using R_{HTM} determined from EIS for devices using mesoporous (mp) TiO_2 (red) or ZrO_2 (blue) infiltrated with undoped spiro-MeOTAD. The measurements made at different potentials for each temperature are represented by the color scale.

In order to gain a better understanding of the transport properties of spiro-MeOTAD within ssDSCs, the R_{HTM} values extracted from the EIS measurements were used to produce an Arrhenius plot as shown in Figure 7. Both systems consisting of mesoporous TiO_2 and ZrO_2 show a clear linear trend between $1/R_{HTM}$ and $1/T$ (Figure 7), indicating that the Arrhenius relationship holds true and allowing E_A to be determined. Taking into account the spread of the measurements at different applied potentials, 0.34 ± 0.02 and 0.40 ± 0.02 eV was determined as E_A for hole transport within spiro-MeOTAD for the mesoporous TiO_2 and ZrO_2 systems, respectively. These are in relatively good agreement with each other, further indicating that the measured R_{HTM} extracted from the intermediate frequency arc originates from the HTM. Additionally these values are consistent with that found by Rana *et al.*,[34] through the study of the charge transport properties of thermally evaporated thin films of spiro-MeOTAD.

Finally the recombination resistance and the corresponding capacitance were determined from the low-frequency arc in the EIS Nyquist plots, section III in Figure 3a. The recombination resistance, R_{ct}, is the charge transfer resistance related to the recombination of electrons at the TiO_2/HTM interface. At low potentials the TiO_2 is an insulator, and hence R_{ct} is high. As the applied potential increases, the electron density within the TiO_2 increases, shifting its Fermi level closer to the lower edge of the conduction band, thus resulting in a decrease in R_{ct}. This behavior was observed for the different systems (mesoporous ZrO_2, flat and mesoporous TiO_2), Figure 8. Furthermore R_{ct} decreased as a function of the applied temperature. This same trend is reflected in the observed increase in the dark current as a function of temperature (see Supporting Information Figure 2). Taking into account the correction for the voltage drop due to the overall series resistance, a larger correction for samples with undoped HTM is observed since for these samples the R_{HTM} is larger (see Supporting Information Figure 5). The region of high forward bias presents the largest potential correction due to the higher current passing. This is visible in the change of the slope of the measured dark current in this potential region as shown in Supporting Information Figure 2. Doping the spiro-MeOTAD samples resulted in only a small reduction in R_{ct}. This is further

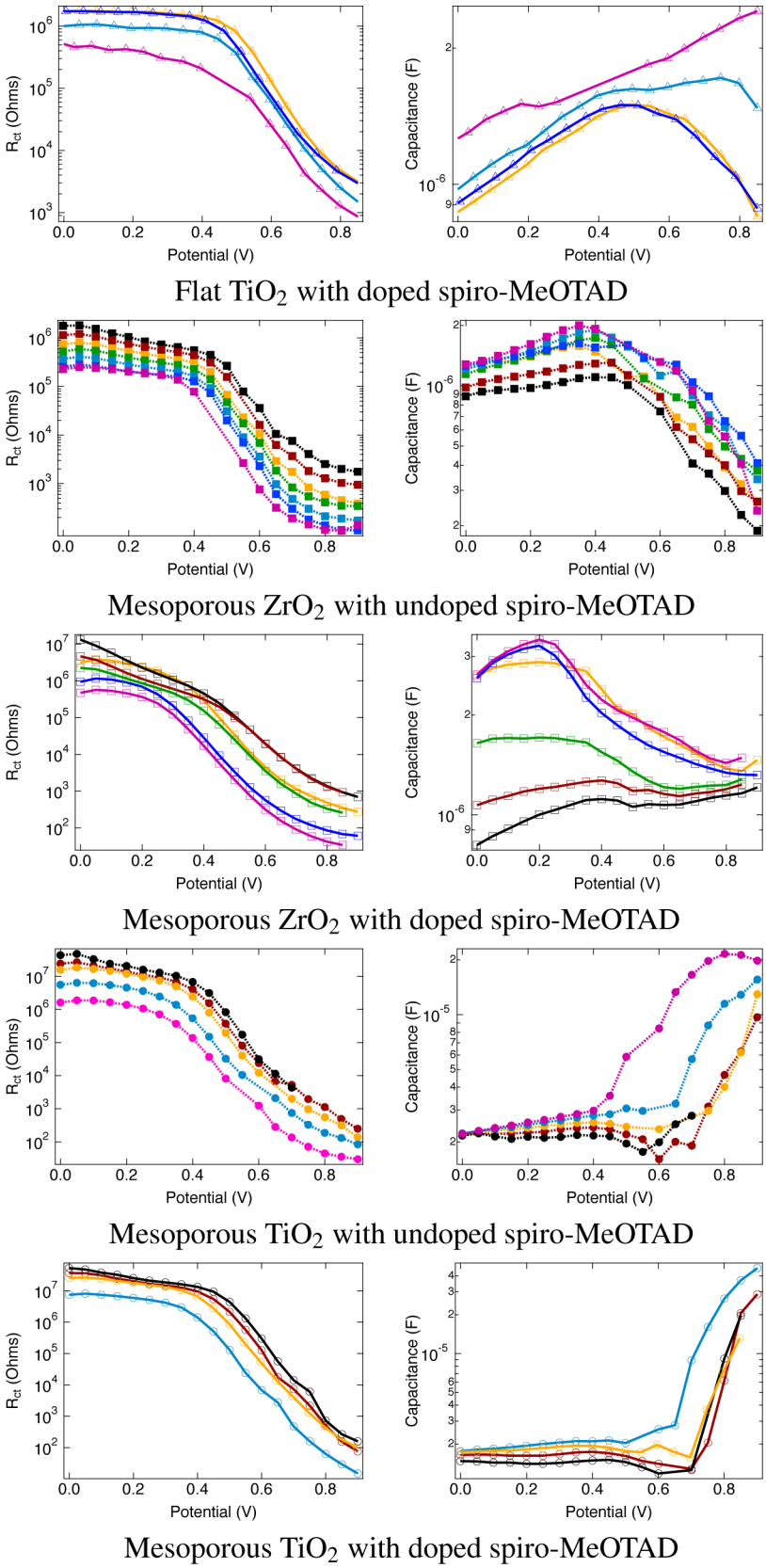

Figure 8. Recombination resistance and the corresponding capacitance for the different systems as a function of potential. Measurement temperatures: black (0 °C), red (10 °C), orange (20 °C), green (30 °C), light blue (40 °C), dark blue (50 °C), magenta (60 °C).

highlighted when R_{ct} is considered in comparison to the chemical capacitance, C_μ (see Figure 9), which shows only a small difference, implying that the electron lifetime and the recombination kinetics within

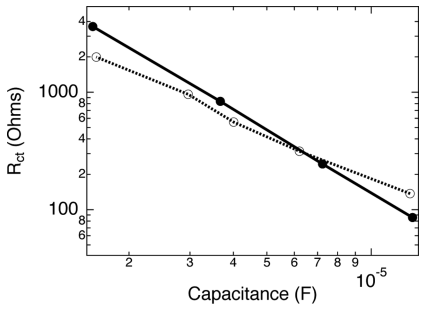

Figure 9. Recombination resistance, R_{ct}, as a function of the chemical capacitance, C_μ, for devices using mesoporous TiO_2 infiltrated with doped (solid line) or undoped (dashed line) spiro-MeOTAD. This set of data corresponds to measurements made at 20 °C. Similar behavior was observed for measurements conducted at other temperatures.

the TiO_2 are mainly unaffected by the p-doping of the spiro-MeOTAD. The electron lifetime, τ_e, is related to the chemical capacitance and the recombination resistance of electrons by

$$\tau_e = C_\mu R_{ct} \quad (2)$$

The capacitance associated with this resistance has been interpreted as the chemical capacitance, C_μ, of the nanostructured materials[35] and has been characterized by an exponential dependence on the applied potential bias. This behavior has been observed experimentally for nanostructured semiconductors and DSCs.[20,36,37] The chemical capacitance has been related to the total electron density, n, within the semiconductor by

$$C_\mu = \frac{e^2}{k_B T} n \quad (3)$$

where e is the electron charge. The chemical capacitance is a critical parameter necessary to understand the underlying mechanisms in DSCs describing the storage of free energy by photogenerated carriers and the resulting production of current and voltage.[35]

Considering the case of the mesoporous TiO_2, the experimentally determined capacitance is found to increase exponentially with potential as expected, displaying a small increase with temperature, Figure 8. Hence this parameter can be interpreted as the chemical capacitance of the nanostructured TiO_2. In previous studies on liquid DSCs C_μ did not show a dependence on temperature.[17] In contrast we observed a temperature dependence of the chemical capacitance as observed by O'Regan *et al.*[38] and Wang *et al.*[39] Thereby the depth of the density of states (DOS) also depends on the temperature. However this effect is rather small in the temperature domain investigated, as visible by the small change in shape of the C_μ. According to O'Regan *et al.*,[38] the main reason for the change of C_μ with temperature is the change in the ionic surrounding of the TiO_2 at elevated temperatures, leading to a displacement of the conduction band edge.

In the case of the mesoporous ZrO_2, the capacitance corresponding to R_{ct} was observed to decrease with potential, however still increasing with temperature. At low temperatures samples using flat TiO_2 showed a similar behavior, where the capacitance displayed a decrease at high potentials. Conversely, at higher temperatures the capacitance indicated an increase at high potentials. It is important to note that the magnitude change in capacitance for this system is small in comparison to the mesoporous systems as a function of potential.

This conflicting behavior can be attributed to the fact that the capacitance measured here is not the chemical capacitance. The interface between the compact TiO_2 and HTM may lead to the formation of a p−n junction, which results in an additional capacitance.[40,41] This is visible in all systems as an increase in the capacitance at approximately 0.4 V. This underlayer capacitance dominates at short-circuit conditions. At high forward bias this type of p−n junction lets charge flow out, preventing further accumulation of charge and thus leading to a decrease in the capacitance. In the case of devices using mesoporous TiO_2, this underlayer capacitance is visible only at lower temperatures; otherwise it is overlaid by the larger chemical capacitance of the mesoporous TiO_2, which increases exponentially as a function of the applied potential.

CONCLUSIONS

The internal electrical processes occurring within ssDSCs using spiro-MeOTAD were investigated using EIS. Particular emphasis was placed upon understanding the transport properties of the HTM within such devices and the role of p-doping the organic semiconductor. The charge transport resistance of spiro-MeOTAD was found to decrease significantly upon chemically p-doping the material. Using the Arrhenius relationship a value for the activation energy corresponding to the hole hopping transport in undoped spiro-MeOTAD was determined. These were found to be in good agreement with values found in the literature, thus demonstrating the validity of the chosen model used to fit the EIS data for these types of systems. R_{HTM} contributes to the overall series resistance of the devices and thus decreases the fill factor. Gaining further understanding of the transport properties of the HTM and methods of its characterization allows more targeted approaches to improve device performance of such ssDSCs.

The choice of mesoporous ZrO_2 as a scaffold for the HTM further allowed the interface between the compact TiO_2 underlayer and the HTM to be scrutinized in a setup identical to nearly working device conditions employing a mesoporous structure. The overall chemical capacitance of the devices was found to show a small increase at approximately 0.4 V originating from

this interface. This is further confirmed by similar behavior observed for the devices utilizing flat TiO_2. These findings suggest the formation of a p−n junction between the compact TiO_2 underlayer and the HTM, which contributes to the overall device capacitance but is frequently masked by the exponential increase in the chemical capacitance arising from the DOS of the mesoporous TiO_2 in conventional working ssDSCs.

In order to isolate the transport properties of spiro-MeOTAD as a HTM in ssDSCs, the analyzed devices did not contain any sensitizer. Now that the behavior of this organic semiconductor is better understood, future work will investigate the effect of including sensitizers in the devices on the transport and interfacial properties of spiro-MeOTAD and consequently on the overall device performance.

METHODS

Device Fabrication. Hydrochloric acid and zinc powder were used to etch fluorine-doped tin oxide glass substrates to achieve the correct electrode configuration. These were subsequently cleaned using ultrasonication in water and ozone treatment. Spray pyrolysis was used to deposit a compact TiO_2 layer using titanium bis(acetylacetonate)diisopropoxide solution in ethanol as a precursor and oxygen as a carrier gas at 450 °C. The substrates were treated with 20 mM titanium tetrachloride ($TiCl_4$) solution at 70 °C for 30 min and sintered for 30 min at 500 °C. Mesoporous ZrO_2 or TiO_2 layers of 2.0−2.2 μm were prepared by screen-printing, before undergoing the previously described $TiCl_4$ treatment again. The pore and particle size of the mesoporous ZrO_2 and TiO_2 used in this study were not identical, which may lead to differences in the pore filling fraction of the films. However the influence of this is outside the scope of this work.

The hole transport material was prepared by dissolving 2,2′,7,7′-tetrakis(*N*,*N*-di-*p*-methoxyphenylamine)-9,9′-spirobifluorene in chlorobenzene to give a 0.15 M solution. For doped samples the Co(III) complex tris(2-(1*H*-pyrazol-1-yl)-pyridine)cobalt(III), coded FK-102,[27] was added to the HTM solution as a p-type dopant to give 1.5% doping of spiro-MeOTAD. Furthermore 0.12 M 4-*tert*-butylpyridine and 0.02 M lithium bis(trifluoromethylsulfonyl)imide (predissolved in acetonitrile) were added to the HTM solution. A 40 μL portion of this solution was deposited onto the mesoporous ZrO_2 or TiO_2 films and allowed to infiltrate for 30 s prior to spin coating for 30 s at 2000 rpm. In the case of the flat samples, the HTM solution used was 0.25 M and deposited directly onto the compact TiO_2 layer. Finally 200 nm thick silver counter electrodes were thermally evaporated onto the films, completing the cell fabrication. The devices were fabricated and sealed under dry atmosphere and red light.

Electrochemical Impedance Spectroscopy. The electrochemical impedance measurements were performed using an Autolab PG30 potentiostat. A dc potential bias was applied and overlaid by a sinusoidal ac potential perturbation of 10 mV over a frequency range of 1 MHz to 0.1 Hz. The applied dc potential bias was changed by 50 mV steps from 850 mV to 0 mV. This set of measurements was repeated for each sample set at different temperatures. All measurements were carried out in the dark. The resulting impedance spectra were fitted using the ZView software (Scribner Associates Inc.).

The *IR*-drop-corrected potential from the potential drop over the total series resistance was calculated according to following procedure: the real potential (V) applied to the TiO_2 was determined by the subtraction of the voltage drop (V_{Drop}) from the externally applied potential ($V_{applied}$). The voltage drop is calculated by the integration of the sum of all series resistances ($R_{Aseries}$) over the current passed ($V = V_{applied} - V_{Drop}$; with $V_{Drop} = \int R_{Aseries}\, dI$, whereby $R_{Aseries} = R_s + R_C + R_{HTM}$).

Conflict of Interest: The authors declare no competing financial interest.

Acknowledgment. The authors thank P. Comte for the preparation of the mesoporous ZrO_2 films. This work was funded by the European Community's Seventh Framework Programme (FP7/2007−2013) under the "ORION" grant agreement no. nmP-229036 and "SANS" agreement no. 246124. This work was supported by the ECR Advanced Grant Agreement no. 247404 under the CE-Mesolight project funded by the European Community's Seventh FWP.

Supporting Information Available: Transport resistance extracted using the transmission line model for a mesoporous TiO_2 sample with undoped spiro-MeOTAD conducted at 60 °C. Dark current measured during EIS measurements for mesoporous ZrO_2 and TiO_2 with undoped spiro-MeOTAD. All resistances and corresponding capacitances presented plotted as a function of the corrected potential. This material is available free of charge *via* the Internet at http://pubs.acs.org/.

REFERENCES AND NOTES

1. O'Regan, B.; Grätzel, M. A Low-Cost, High-Efficiency Solar Cell Based on Dye-Sensitized Colloidal TiO_2 Films. *Nature* **1991**, *353*, 737–740.
2. Yella, A.; Lee, H. W.; Tsao, H. N.; Yi, C.; Chandiran, A. K.; Nazeeruddin, M. K.; Diau, E. W. G.; Yeh, C. Y.; Zakeeruddin, S. M.; Grätzel, M. Porphyrin-Sensitized Solar Cells with Cobalt (II/III)-Based Redox Electrolyte Exceed 12% Efficiency. *Science* **2011**, *334*, 629–634.
3. Kroeze, J. E.; Hirata, N.; Schmidt-Mende, L.; Orizu, C.; Ogier, S. D.; Carr, K.; Grätzel, M.; Durrant, J. R. Parameters Influencing Charge Separation in Solid-State Dye-Sensitized Solar Cells Using Novel Hole Conductors. *Adv. Funct. Mater.* **2006**, *16*, 1832–1838.
4. Juozapavicius, M.; O'Regan, B.; Anderson, A. Y.; Grazulevicius, J. V.; Mimaite, V. Efficient Dye Regeneration in Solid-State Dye-Sensitized Solar Cells Fabricated with Melt Processed Hole Conductors. *Org. Electron.* **2012**, *13*, 23–30.
5. Leijtens, T.; Ding, I. K.; Giovenzana, T.; Bloking, J. T.; McGehee, M. D.; Sellinger, A. Hole Transport Materials with Low Glass Transition Temperatures and High Solubility for Application in Solid-State Dye-Sensitized Solar Cells. *ACS Nano* **2012**, *6*, 1455–1462.
6. Unger, E. L.; Morandeira, A.; Persson, M.; Zietz, B.; Ripaud, E.; Leriche, P.; Roncali, J.; Hagfeldt, A.; Boschloo, G. Contribution From a Hole-Conducting Dye to the Photocurrent in Solid-State Dye-Sensitized Solar Cells. *Phys. Chem. Chem. Phys.* **2011**, *13*, 20172–20177.
7. Hsu, C.-Y.; Chen, Y.-C.; Lin, R. Y.-Y.; Ho, K.-C.; Lin, J. T. Solid-State Dye-Sensitized Solar Cells Based on Spirofluorene (Spiro-OMeTAD) and Arylamines as Hole Transporting Materials. *Phys. Chem. Chem. Phys.* **2012**, *14*, 14099–14109.
8. Tennakone, K.; Kumara, G. R. R. A.; Kumarasinghe, A. R.; Wijayantha, K. G. U.; Sirimanne, P. M. A Dye-Sensitized Nanoporous Solid-State Photovoltaic Cell. *Semicond. Sci. Technol.* **1999**, *10*, 1689–1693.
9. Chung, I.; Lee, B.; He, J.; Chang, R. P. H.; Kanatzidis, M. G. All-Solid-State Dye-Sensitized Solar Cells with High Efficiency. *Nature* **2012**, *485*, 486–489.
10. Tsujimoto, K.; Nguyen, D.-C.; Ito, S.; Nishino, H.; Matsuyoshi, H.; Konno, A.; Kumara, G. R. A.; Tennakone, K. TiO_2 Surface Treatment Effects by Mg^{2+}, Ba^{2+}, and Al^{3+} on Sb_2S_3 Extremely Thin Absorber Solar Cells. *J. Phys. Chem. C* **2012**, *116*, 13465–13471.
11. Zhang, W.; Zhu, R.; Li, F.; Wang, Q.; Liu, B. High-Performance Solid-State Organic Dye Sensitized Solar Cells with P3HT as Hole Transporter. *J. Phys. Chem. C* **2012**, *115*, 7038–7043.

12. Zhang, W.; Cheng, Y.; Yin, X.; Liu, B. Solid-State Dye-Sensitized Solar Cells with Conjugated Polymers as Hole-Transporting Materials. *Macromol. Chem. Phys.* **2011**, *212*, 15–23.
13. Bach, U.; Lupo, D.; Comte, P.; Moser, J.-E.; Weissortel, F.; Salbeck, J.; Spreitzer, H.; Grätzel, M. Solid-State Dye-Sensitized Mesoporous TiO_2 Solar Cells with High Photon-to-Electron Conversion Efficiencies. *Nature* **1998**, *395*, 583–585.
14. Minna, T.; Janne, H.; Lauri, P.; Peter, L. Investigation of Temperature and Aging Effects in Nanostructured Dye Solar Cells Studied by Electrochemical Impedance Spectroscopy. *Int. J. Photoenergy* **2009**, *2009*, 1–15.
15. Wang, Q.; Moser, J.-E.; Grätzel, M. Electrochemical Impedance Spectroscopic Analysis of Dye-Sensitized Solar Cells. *J. Phys. Chem. B* **2005**, *109*, 14945–14953.
16. Toivola, M.; Peltokorpi, L.; Halme, J.; Lund, P. Regenerative Effects by Temperature Variations in Dye-Sensitized Solar Cells. *Sol. Energy Mater. Sol. Cells* **2007**, *91*, 1733–1742.
17. Wang, Q.; Ito, S.; Grätzel, M.; Fabregat-Santiago, F.; Mora-Sero, I.; Bisquert, J.; Bessho, T.; Imai, H. Characteristics of High Efficiency Dye-Sensitized Solar Cells. *J. Phys. Chem. B* **2006**, *110*, 25210–25221.
18. Góes, M. S.; Joanni, E.; Muñiz, E. C.; Savu, R.; Habeck, T. R.; Bueno, P. R.; Fabregat-Santiago, F. Impedance Spectroscopy Analysis of the Effect of TiO_2 Blocking Layers on the Efficiency of Dye Sensitized Solar Cells. *J. Phys. Chem. C* **2012**, *116*, 12415–12421.
19. Bisquert, J.; Fabregat-Santiago, F.; Mora-Sero, I.; Garcia-Belmonte, G.; Gimenez, S. Electron Lifetime in Dye-Sensitized Solar Cells: Theory and Interpretation of Measurements. *J. Phys. Chem. C* **2009**, *113*, 17278–17290.
20. Fabregat-Santiago, F.; Garcia-Belmonte, G.; Bisquert, J.; Zaban, A.; Salvador, P. Decoupling of Transport, Charge Storage, and Interfacial Charge Transfer in the Nanocrystalline TiO_2/Electrolyte System by Impedance Methods. *J. Phys. Chem. B* **2002**, *106*, 334–339.
21. Bisquert, J.; Garcia-Belmonte, G.; Fabregat-Santiago, F.; Compte, A. Anomalous Transport Effects in the Impedance of Porous Film Electrodes. *Electrochem. Commun.* **1999**, *1*, 429–435.
22. Fabregat-Santiago, F.; Bisquert, J.; Cevey-Ha, N.-L.; Chen, P.; Wang, M.; Zakeeruddin, S. M.; Grätzel, M. Electron Transport and Recombination in Solid-State Dye Solar Cell with Spiro-OMeTAD as Hole Conductor. *J. Am. Chem. Soc.* **2008**, *131*, 558–562.
23. Fabregat-Santiago, F.; Bisquert, J.; Palomares, E.; Haque, S. A.; Durrant, J. R. Impedance Spectroscopy Study of Dye-Sensitized Solar Cells with Undoped Spiro-OMeTAD as Hole Conductor. *J. Appl. Phys.* **2006**, *100*, 034510.
24. Snaith, H.; Grätzel, M. Enhanced Charge Mobility in a Molecular Hole Transporter Via Addition of Redox Inactive Ionic Dopant: Implication to Dye-Sensitized Solar Cells. *Appl. Phys. Lett.* **2006**, *89*, 262114.
25. Abate, A.; Leijtens, T.; Pathak, S.; Teuscher, J.; Avolio, R.; Errico, M. E.; Kirkpatrik, J.; Ball, J. M.; Docampo, P.; McPherson, I.; *et al.* Lithium Salts As "Redox Active" p-Type Dopants for Organic Semiconductors and Their Impact in Solid-State Dye-Sensitized Solar Cells. *Phys. Chem. Chem. Phys.* **2013**, 10.1039/c2cp44397j.
26. Cappel, U. B.; Daeneke, T.; Bach, U. Oxygen-Induced Doping of Spiro-MeOTAD in Solid-State Dye-Sensitized Solar Cells and Its Impact on Device Performance. *Nano Lett.* **2012**, *12*, 4925–4931.
27. Burschka, J.; Dualeh, A.; Kessler, F.; Baranoff, E.; Cevey-Ha, N.-L.; Yi, C.; Nazeeruddin, M. K.; Grätzel, M. Tris(2-(1H-pyrazol-1-yl)pyridine)cobalt(III) as p-Type Dopant for Organic Semiconductors and Its Application in Highly Efficient Solid-State Dye-Sensitized Solar Cells. *J. Am. Chem. Soc.* **2012**, *133*, 18042–18045.
28. Boix, P. P.; Lee, Y. H.; Fabregat-Santiago, F.; Im, S. H.; Mora-Sero, I.; Bisquert, J.; Seok, S. I. From Flat to Nanostructured Photovoltaics: Balance between Thickness of the Absorber and Charge Screening in Sensitized Solar Cells. *ACS Nano* **2012**, *6*, 873–880.
29. Boix, P. P.; Larramona, G.; Jacob, A.; Delatouche, B.; Mora-Sero, I.; Bisquert, J. Hole Transport and Recombination in All-Solid Sb_2S_3-Sensitized TiO_2 Solar Cells Using CuSCN As Hole Transporter. *J. Phys. Chem. C* **2012**, *116*, 1579–1587.
30. Snaith, H.; Humphry-Baker, R.; Chen, P.; Cesar, I.; Zakeeruddin, S. M.; Grätzel, M. Charge Collection and Pore Filling in Solid-State Dye Sensitized Solar Cells. *Nanotechnology* **2008**, *19*, 424003.
31. Cai, N.; Moon, S.-J.; Cevey-Ha, N.-L.; Moehl, T.; Humphry-Baker, R.; Wang, P.; Zakeeruddin, S. M.; Grätzel, M. An Organic D-Pi-A Dye for Record Efficiency Solid-State Sensitized Heterojunction Solar Cells. *Nano Lett.* **2012**, *11*, 1452–1456.
32. Bisquert, J.; Grätzel, M.; Wang, Q.; Fabregat-Santiago, F. Three-Channel Transmission Line Impedance Model for Mesoscopic Oxide Electrodes Functionalized with a Conductive Coating. *J. Phys. Chem. B* **2006**, *110*, 11284–11290.
33. Bach, U.; De Cloedt, K.; Spreitzer, H.; Grätzel, M. Characterization of Hole Transport in a New Class of Spiro-Linked Oligotriphenylamine Compounds. *Adv. Mater.* **2000**, *12*, 1060–1063.
34. Rana, O.; Srivastava, R.; Grover, R.; Zulfequar, M.; Husain, M.; Kamalasanan, M. N. Charge Transport Studies in Thermally Evaporated 2,2′,7,7′-Tetrakis-(*N*,*N*-di-4-methoxyphenylamino)-9,9′-spirobifluorene (Spiro-MeOTAD) Thin Film. *Synth. Met.* **2011**, *161*, 828–832.
35. Bisquert, J. Chemical Capacitance of Nanostructured Semiconductors: its Origin and Significance for Nanocomposite Solar Cells. *Phys. Chem. Chem. Phys.* **2003**, *5*, 5360–5364.
36. van de Lagemaat, J.; Frank, A. J. Effect of the Surface-State Distribution on Electron Transport in Dye-Sensitized TiO_2 Solar Cells: Nonlinear Electron-Transport Kinetics. *J. Phys. Chem. B* **2000**, *104*, 4292–4294.
37. Fabregat-Santiago, F.; Bisquert, J.; Garcia-Belmonte, G.; Boschloo, G.; Hagfeldt, A. Influence of Electrolyte in Transport and Recombination in Dye-Sensitized Solar Cells Studied by Impedance Spectroscopy. *Sol. Energy Mater. Sol. Cells* **2005**, *87*, 117–131.
38. O'Regan, B.; Durrant, J. R. Calculation of Activation Energies for Transport and Recombination in Mesoporous TiO_2/Dye/Electrolyte Films Taking into Account Surface Charge Shifts with Temperature. *J. Phys. Chem. B* **2006**, *110*, 8544–8547.
39. Cao, Y.; Bai, Y.; Yu, Q.; Cheng, Y.; Liu, S.; Shi, D.; Gao, F.; Wang, P. Dye-Sensitized Solar Cells with a High Absorptivity Ruthenium Sensitizer Featuring a 2-(Hexylthio)thiophene Conjugated Bipyridine. *J. Am. Chem. Soc.* **2009**, *113*, 6290–6297.
40. Bisquert, J.; Cahen, D.; Hodes, G.; Rühle, S.; Zaban, A. Physical Chemical Principles of Photovoltaic Conversion with Nanoparticulate, Mesoporous Dye-sensitized Solar Cells. *J. Phys. Chem. B* **2004**, *108*, 8106–8118.
41. Fabregat-Santiago, F.; Garcia-Belmonte, G.; Mora-Sero, I.; Bisquert, J. Characterization of Nanostructured Hybrid and Organic Solar Cells by Impedance Spectroscopy. *Phys. Chem. Chem. Phys.* **2011**, *13*, 9083–9118.